Supplemental materials: Fluctuation spectroscopy of giant unilamellar vesicles using confocal and phase contrast microscopy

Hammad A. Faizi,[ab] Cody J. Reeves,[c], Vasil N. Georgiev[b], Petia M. Vlahovska,[ac] and Rumiana Dimova*[b]
[a] *Department of Mechanical Engineering, Northwestern University, Evanston, IL 60208, USA*
[b] *Department of Theory and Biosystems, Max Planck Institute of*
Colloids and Interfaces, Science Park Golm, 14424 Potsdam, Germany.
[c] *Department of Engineering Sciences and Applied Mathematics,*
Northwestern University, Evanston, IL 60208, USA.
∗ *E-mails for correspondence Rumiana.Dimova@mpikg.mpg.de, Petia.Vlahovska@northwestern.edu*

(Dated: September 21, 2020)

S1. Bending rigidity value of DOPC bilayers

The bending rigidity values of bilayer membranes made of the same lipid can vary across studies due to different conditions, e.g., sugars, salt, buffers, dye concentration, as well as the preparation method [1]. Table I illustrates the wide range of reported values of the bending rigidity values DOPC bilayers. Refer to Table II for the bending rigidity values obtained in this study for different microscopy setting.

TABLE I: Different bending rigidity values for DOPC under different conditions and methods.PC, C and EP refer to phase contrast, confocal and epi-flourescent microscopies used respectively in Fluctuation spectroscopy.

Method	Rigidity (k_BT)	Dye conc. (%*mol*)	Buffer, Sugar (inside/outside)	Salt	Preparation
Fluctuation Spec. [EP,C]	14.9±0.4 [2]	15.8 NBD PC	100 mM Sucrose/100 mM Sucrose	N/A	Electroformation
Fluctuation Spec. [PC]	26.4±2.4 [3]	0 or 0.1 diIC18	10 mM Sucrose/10 mM Glucose	0.1 mM NaCl	Electroformation
Fluctuation Spec. [PC]	26.8±2.4 [4]	1.0 Liss Rhod PE	450 mM Sucrose/500 mM Glucose	N/A	Electroformation
Fluctuation Spec. [PC]	29.8±2.4 [4]	1.0 Liss Rhod PE	450 mM Sucrose/500 mM Glucose	N/A	Phase Transfer
Fluctuation Spec. [EP]	22.3±0.5 [5]	0.12 Liss Rhod PE	100 mM Sucrose/200 mM Sucrose	N/A	Electroformation
Fluctuation Spec. [PC]	27.3±3.2 [6]	N/A	100 mM Sucrose/100 mM Sucrose	2 mM NaN_3	Electroformation
Fluctuation Spec. [PC]	22.7±2 [7]	N/A	100 mM Sucrose/125 mM Glucose	N/A	Electroformation
Fluctuation Spec. [PC]	21.46±4 [8]	N/A	100 mM Sucrose/125 mM Glucose	N/A	Electroformation
Fluctuation Spec. [PC]	19±1 [9]	N/A	10 mM Sucrose/10 mM Glucose	N/A	Electroformation
Fluctuation Spec. [C]	19±1 [10]	0.8 TR DHPE	197 mM Sucrose/200 mM Glucose	N/A	Electroformation
Time Correlations	22.1 [11]	N/A	300 mM Sucrose/307 mM Glucose	N/A	Electroformation
Micropipette Aspiration	20.7±2 [12]	N/A	100 mM Sucrose/100 mM Glucose	N/A	Thin Film Hyd.
Micropipette Aspiration	22.8±2.2 [9]	N/A	8 mM Sucrose/8 mM Glucose	N/A	Electroformation
X- Ray Scattering	20±2 [13]	N/A	Water/Water	N/A	Extrusion
X- Ray Scattering	20.2±1.4 [14]	N/A	Deionized water	N/A	Bilayer stack
Electrodeformation	21.9±2 [3]	0.1 diIC18	10 mM Sucrose/10 mM Glucose	0.1 mM NaCl	Electroformation
Tether pulling	20±2 [15]	0.3 TR DHPE	300 mM Sucrose/80 mM Glucose	100 mM NaCl	Electroformation
Neutron Spin Echo	20±1 [16]	N/A	D_2O/D_2O	0 mM	Extrusion
Neutron Spin Echo	20±2 [17]	N/A	D_2O/D_2O	0 mM	Extrusion
Neutron Spin Echo	30±4 [17]	N/A	D_2O/D_2O	150 mM	Extrusion
Neutron Spin Echo	40±5 [17]	N/A	D_2O/D_2O	470 mM	Extrusion
Interferometry	10.5±8.8 [18]	N/A	295 mM Sucrose/300 mM Glucose	N/A	Electroformation

TABLE II: Bending rigidity values obtained in this study for DOPC under different conditions and microscopy settings. Note the sugar concentration is the same in all the experiments: 20 mM Sucrose inside/ 22 mM Glucose outside. The dye used is TR DHPE and all the vesicles were formed via electroformation.

Microscopy	Rigidity ($k_B T$)	Dye conc. ($\% mol$)	Objective/NA	Polarization Correction	Pinhole (A.U)
Phase Contrast	19.4±2.1	0.2	100x/1.25	N/A	N/A
Phase Contrast	22.5±1.5	0	40x/0.6	N/A	N/A
Phase Contrast	23.3±1.6	0.2	40x/0.6	N/A	N/A
Phase Contrast	21.0±2.0	0.2	40x/1.3	N/A	N/A
Confocal	21.7±2.0	0.2	40x/1.3	Yes	1
Confocal	22.5±2.1	0.2	40x/0.6	Yes	1
Confocal	22.5±2.4	0.2	40x/0.6	Yes	0.3
Confocal	22.6±3.5	0.2	40x/0.6	Yes	2
Confocal	20.4±4.0	0.2	40x/0.6	No	1
Confocal	22.3±1.6	0.2	40x/1.3	No	1
Confocal	25.0±2.1	2.0	40x/0.6	Yes	1

S2. Methods

Vesicle preparation

Giant unilamellar vesicles (GUVs) were prepared using the classical electroformation method [19] from DOPC and the fluorescent lipid Texas Red 1,2-hexadecanoyl-sn-glycero-3-phosphoethanolamine (TR-DHPE). The composition of the GUVs explored are 99.8 % DOPC 0.2 % TR-DHPE and 98 % DOPC 2 % TR-DHPE (mole fractions). Stock solutions of DOPC and TR-DHPE at 10 mg/ml and 1 mg/ml in chloroform were diluted to a final concentration of 4 mM for varying proportions. A small volume, 10 μl, of the solution was spread on the conductive surface of two glass slides coated with indium tin oxide (ITO) (Delta Technologies). The glass slides were then stored under a vacuum for 1–2 hours to remove traces of organic solvent. Afterwards, a 2 mm Teflon spacer was sandwiched between the glass slides and the chamber was gently filled with 20 mM sucrose solution. The slides (conductive side facing inward) were connected to an AC signal generator Agilent 33220A (Agilent Technology GmbH, Germany). An AC field of voltage 1.5 V and frequency 10 Hz applied for 2 hours at room temperature, resulting in 10-50 μm sized vesicles. The harvested vesicles were diluted 10 times in 22 mM glucose solution to obtain fluctuating vesicles. All GUVs were analyzed within 8 hours of electoformation.

Microscopy and video recording

The equatorial fluctuations for both phase contrast and confocal mode were recorded with Leica TCS SP8 scanning confocal microscope using a HCX PL APO 40x/ Numerical Aperture (NA) 0.6 Ph2 (air) objective and a HC PL APO 40x/ NA 1.3 (oil) objective. The pinhole size during the experiment was fixed to 1 AU (Airy units) unless stated otherwise. Table 1 compiles the pixel size and focal depth for different experimental conditions. The scanning speed was fixed to 1 kHz in bidirectional mode and the polarizer plates were rotated (100%) to remove the polarization effect of the fluorescent dye unless stated otherwise. The dye was excited with a 561 nm laser (diode-pumped solid-state laser) with 1.61% (laser intensity) HyD3 detector (hybrid) and the gain was fixed to 23%. Phase contrast imaging was recorded with PCO CS dimax (PCO AG, Kelheim, Germany)) mounted on confocal microscope. 1500-2000 images were recorded at 3.83 frames per second (fps) with confocal and 60 fps with phase contrast imaging. The RGB confocal images were converted to 8 bit and then inverted. We implemented an inbuilt MATLAB sobel disk filter $fspecial('sobel')$ and image normalization to increase the contrast of the contour.

In this section, we list different focal depths and pixel sizes for different microscopy and numerical aperture settings for 40x objective. Focal depth or FWHM (full width half maximum) of phase contrast imaging was determined using the standard formula $d = \frac{\lambda}{NA^2}$ The wavelength of transmission light was assumed to be 550 nm.

TABLE III: Different experimental conditions for video recording with 40x objective.

Microscopy	Numerical Aperture	Medium	Pinhole size (AU)	Focal depth (μm)	Pixel Resolution (nm)
Phase contrast	0.6	Air	1	1.57	276.9
Phase contrast	1.3	Oil	1	0.35	158.7
Confocal	0.6	Air	1	1.61	252.7
Confocal	1.3	Oil	1	0.52	252.7

TABLE IV: Focal depth or FWHM (full width half maximum) for confocal imaging.

Medium	Pinhole size (AU)	Focal depth (μm)
Air	0.3	0.9
Air	1	1.6
Air	2	2.9

Sub-pixel contour recognition

The intensity profile in the radial direction for N wedges were determined from three different interpolation schemes (Gaussian, parabolic and linear weighting of neighbouring pixel) for sub-pixel contour recognition. This was done to check if different interpolation schemes affects the bending rigidity values due to uncertainty introduced at higher wave-numbers for experimental vesicle contour fluctuations. The mean bending rigidity obtained was similar for all the three schemes for the same vesicle. Figure (S1) illustrates the subpixel accuracy determination for a 35 μm radius vesicle. The bending rigidities obtained was 22.0±3.0 k_BT, 21.1±1.0 k_BT and 21.9±2.2 k_BT from Gaussian, parabolic and linear interpolation schemes respectively.

S3. Polarization Effects

We analyzed the same vesicle with and without polarization effects. The polarization effects were corrected using circular plates that were rotated 100%. Figure (S2) illustrates the effect of dye polarization for vesicles imaged with different numerical apertures. Using one Anova test, we find a significant difference of 3 k_BT for the 40x/0.6 NA case. The difference tends to be negligible for 40x/1.3 NA case.

S4. Effect of Vesicle Size on Bending Rigidity Values

The bending rigidity obtained from confocal microscopy with low-resolution optics (e.g. 40x objective, NA 0.6, 1 AU, polarization correction) can be systematically underestimated if the vesicle population contains similar sized vesicles. We demonstrate this by comparing the bending rigidity of the same vesicle imaged with confocal and phase-contrast microscopy, see Figure (S3). Vesicles with smaller sizes yield apparently lower bending rigidity, see Fig. S4 which further highlights the bias effect. For small vesicles, the out-of-focus signal gives rise to asymmetry in the contour intensity (illustrated in Fig. 4a in the main text) which leads to errors in the contour detection and underestimation of the bending rigidity. When the refractive index difference across the membrane is small (as is the case in our experiments), phase contrast imaging does not suffer from this size bias.

S5. Bootstrapping resampling

Details about the various statistical techniques can be found in Ref. [20]. Here we explain the bootstrapping sampling technique. A more rigorous reference is the textbook [21]. In practice, the finite amount of data or length of experiment limits the accuracy to infer data confidently. Bootstrapping is an inference method about the population from a given sample. In bootstrap-resamples, the population is in fact the sample and this quantity is known. This allows to measure the quality of inference of the 'true' sample from a re-sampled data. For example, let's consider the average mass of the human population world wide. It is difficult to measure the mass of every individual globally, therefore, a small sample is measured. Let's assume the sample size of N people. From that sample size, only one mean can be measured. In order to have a reasonable estimate about the population statistics, we need to have variability

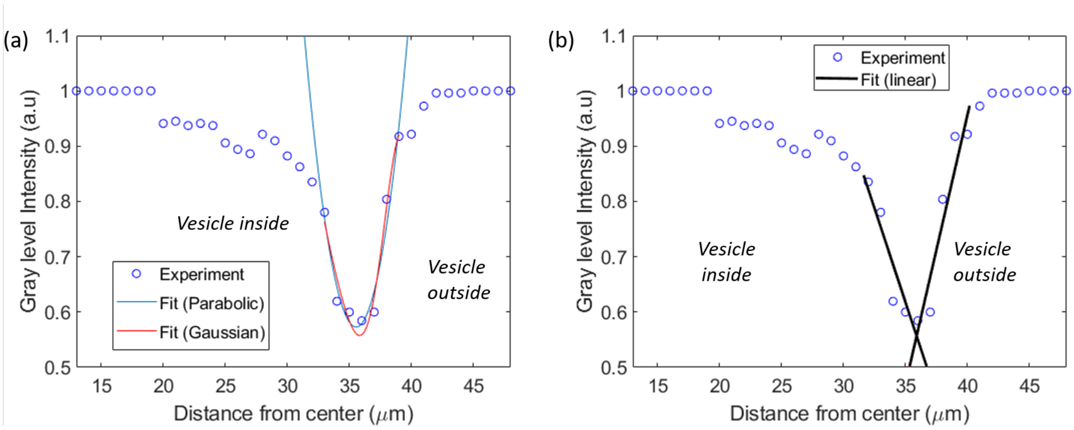

Fig. S 1: Intensity profile for a vesicle contour obtained from confocal imaging. The contour recognition details are given in [3]. The sub-pixel accuracy of the contour profile is determined based on (a) Gaussian, parabolic and (b) linear interpolations

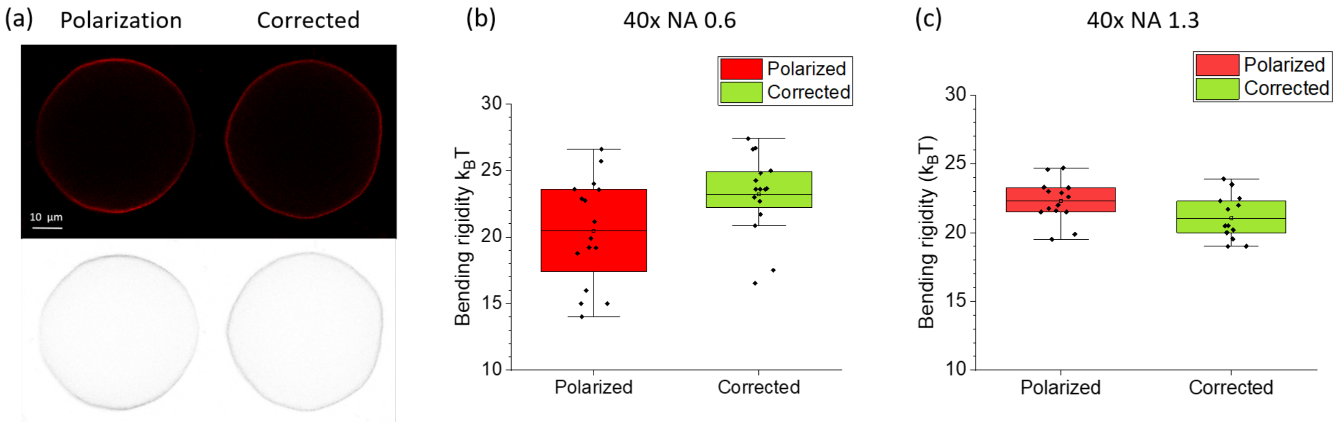

Fig. S 2: Polarization effects. (a) Confocal images of the same vesicle with and without polarization effects for 40x/0.6 NA case. The polarization effects were removed using circular plates that were rotated 100%. (b, c) Comparison between the same vesicles for different numerical apertures. Using one Anova test, we find a significant difference of 3 k_BT for 40x/0.6 NA case. The difference tends to be negligible for 40x/1.3 NA case. Pinhole size is 1 AU.

of the mean that we computed. The simplest bootsampling statistics can be considered by taking the original data N individuals and resampling to create a new sample of the same size N (e.g. we might 'resample' 10 times from [60,61,62,63,64,65,66,67] kg and get [61,64,63,63,60,60,62,65] kg). This process is repeated a large number of times, 100 to 10000, to create a histogram that be applied to any estimator testing. Bootstrap resampling was carried out using MATLAB's *bootstrp ()*.

In the case of our experiments, the finite amount of data or length of experiment limits the accuracy to infer data confidently. The bootstrap resampling requires choosing random replacement from a given data set and examining each sample the same way. This way a particular data point from the original set can reappear randomly multiple times in a particular bootstrap sample. The element size of the bootstrap sample is the same as the element size of the original data. This technique allows to obtain uncertainty of the quantity one estimates.

Bootstrap resampling algorithm for estimating standard error [21]:
1. Obtain N independent bootstrap samples $X^{*1}, X^{*2}, X^{*3}, ...X^{*N}$, each consisting of n data values drawn with a replacement from x where $x = [x^1, x^2, x^3...x^n]$. Note for estimating a standard error, the number N will ordinarily be larger than 30 to satisfy the Central Limit Theorem. Computations allow to use a large number N such as 10^3 to 10^4.
2. Determine the bootstrap replication for every bootstrap resample:

$$\zeta^*(b) = s(X^{*b}) \qquad b = [1, 2, 3, ..N] \tag{1}$$

where $s()$ is a statistical function like sample mean. For example, if $s(x)$ is the sample mean $\bar{x}$ then $S(X^*)$ is the

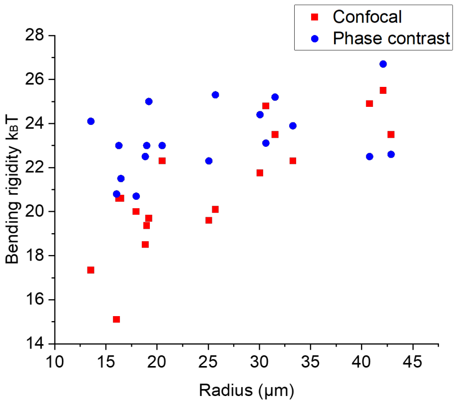

Fig. S 3: Vesicle size effects. Every vesicle was imaged with confocal and phase contrast microscopy. Data are collected on DOPC vesicles with different sizes. The dye concentration was 0.2 mol. Imaging was done with 40x objectives with NA 0.6, 1 AU and polarization correction.

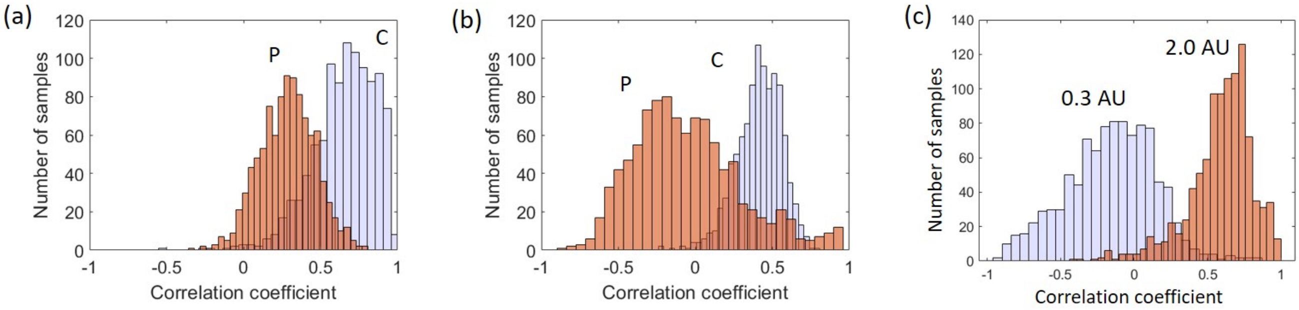

Fig. S 4: Bootstrap method with 95% confidence to evaluate bending rigidity dependence on size of vesicles for different numerical aperture (a) 40x/0.6 NA, (b) 40x/1.3 NA in phase contrast (P) or confocal(C) microcopy, and the pinhole sizes (c) (blue AU 0.3 and red AU 2).

mean of bootstrap data set.
3. Compute the standard error SE by utilizing the standard deviation of N replications

$$SE = \left[\frac{\sum_{b=1}^{N} [\zeta^*(b) - \zeta^*(.)]}{N-1} \right]^{\frac{1}{2}} \tag{2}$$

where $\zeta^*(.) = \sum_{b=1}^{N} \zeta^*(b)/N$.

In our case we determine the SE of mean Pearson correlation using bootsampling statistics.

S6. Numerical simulations of vesicle contours

Mathematical Model

The total energy of the system is given by the Helfrich model[22] as Eq. (3) where κ is the bending rigidity, c_1 and c_2 are the local radii curvatures, A is the total surface area, V is the interior volume of the vesicle, σ is the surface tension, and p is the pressure difference across the membrane.

$$F = \frac{\kappa}{2} \int_A (c_1 + c_2)^2 dA + \sigma A + pV \tag{3}$$

For a quasi-spherical vesicle in equilibrium, the shape can be decomposed into spherical harmonics ($\mathcal{Y}_{lm}$) such that the position of the surface is given by

$$R(\theta,\phi,t) = R_0\left(1+\sum_{l=0}^{l_{max}}\sum_{m=-l}^{l} f_{lm}(t)\mathcal{Y}_{lm}(\theta,\phi)\right) \tag{4}$$

where the characteristic radius R_0 is given by $V=\frac{4}{3}\pi R_0^3$. The spherical harmonics are defined as

$$\mathcal{Y}_{lm} = n_{lm}P_{lm}(\cos\theta)e^{\mathrm{i}m\phi}\,, \quad n_{lm} = \sqrt{\frac{(2l+1)(l-m)!}{4\pi(l+m)!}} \tag{5}$$

$P_{lm}(\cos\theta)$ are the associated Legendre polynomials.

As $l=1$ account for translational modes, for the sake of this paper, $f_{lm}(t)$ will be restricted to $f_{1m}(t)=0$ for $l=1$. Furthermore, volume conservation requires that [23]

$$f_{00} = \frac{-1}{\sqrt{4\pi}}\sum_{l=2}^{l_{max}}\sum_{m=-l}^{l}|f_{lm}|^2. \tag{6}$$

Assuming there is no external fluid flow, the harmonic coefficients (f_{lm}) for $l>1$ are described by the following stochastic differential equation [23]

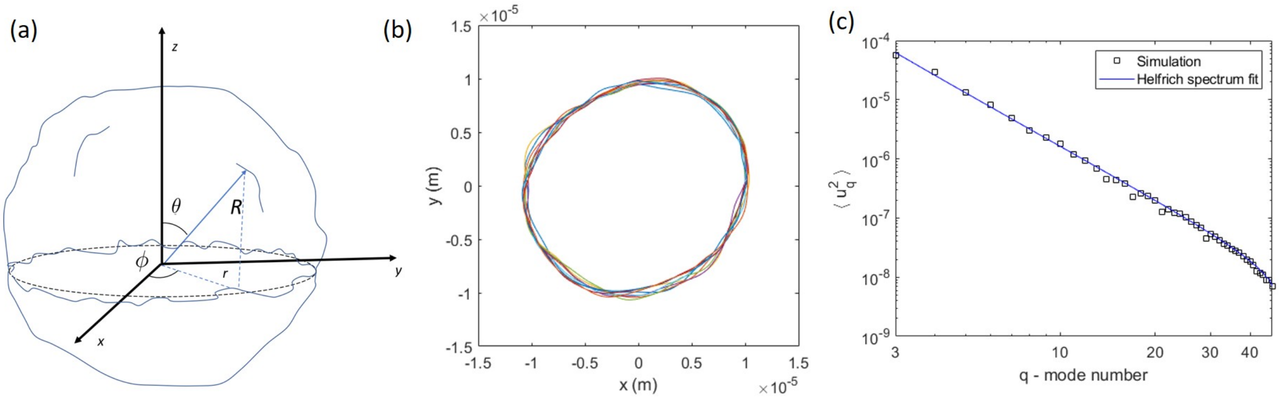

Fig. S 5: (a) A sketch of a GUV. (b) Time sequence of vesicle contours taken at time intervals of 1 s; the bending rigidity is $\kappa = 1\times 10^{-19}$ J and the membrane tension is $\sigma = 1\times 10^{-9}$ N/m. The size of the vesicle is $R_0 = 10^{-5}$ m. (c) Helfrich mode spectrum determined by the image detecting algorithm based on Ref. [3]. The spectrum was fitted with Equation 2 from the main text to obtain the bending rigidity and membrane tension.

$$\partial_t f_{lm} = -\tau_l^{-1} f_{lm} + \zeta_{lm}(t) \tag{7}$$

where

$$\tau_l = \frac{\eta_{\mathrm{ex}}R_0^3}{\kappa\Gamma_l(\lambda)E_l}, \quad \Gamma_l = \frac{l(l+1)}{4l^3+6l^2-1+\left(2l^3+3l^2-5\right)(\lambda-1)} \quad \text{and} \quad E_l = (l+2)(l-1)\Big(l(l+1)+\bar{\sigma}\Big). \tag{8}$$

A tutorial derivation of the evolution equation and the relaxation time (in the absence of thermal noise) can be found in Refs. [24, 25] The dimensionless tension is $\bar{\sigma} = \sigma R_0^2/\kappa$. $\lambda = \eta_{\mathrm{in}}/\eta_{\mathrm{ex}}$ is the ratio of viscosities of the solutions inside and outside the vesicle. When $\lambda = 1$, our result for the relaxation time reduces to the one reported by Refs. [23, 26]. To make easier comparison with the result of Ref. [10], we can rewrite the relaxation time as

$$\tau_l = \frac{R_0^3}{\kappa}\frac{\eta_{\mathrm{ex}}\left(2l^3+3l^2+4\right)+\eta_{\mathrm{in}}\left(2l^3+3l^2-5\right)}{l(l+1)(l+2)(l-1)\Big(l(l+1)+\bar{\sigma}\Big)} \tag{9}$$

$\zeta_{lm}(t)$ is a stochastic term accounting for thermal noise; the corresponding time correlation is given as

$$\Big\langle \zeta_{lm}(t)\zeta_{l'm'}(t')\Big\rangle = (-1)^m\,\frac{2k_BT\Gamma_l}{\eta_{\mathrm{ex}}R_0^3}\,\delta_{l,l'}\delta_{m,-m'}\delta(t-t'). \tag{10}$$

The δ functions are the traditional Kronecker and Dirac delta functions. From Eq. 10, the variance of $\zeta_{lm}(t)$ is given by

$$\left\langle |\zeta_{lm}|^2 \right\rangle = 2\frac{k_B T \Gamma_l}{\eta_{\text{ex}} R_0^3} = 2\Sigma_l. \tag{11}$$

Numerical Method

At this point, it is convenient to decompose f_{lm} and ζ_{lm} into real and imaginary components such that $f_{lm}(t) = X_{lm}(t) + \mathrm{i}\ Y_{lm}(t)$ and $\zeta_{lm}(t) = a_{lm}(t) + \mathrm{i}\ b_{lm}(t)$. As a_{lm} and b_{lm} are independent of each other then

$$\left\langle |\zeta_{lm}|^2 \right\rangle = \left\langle |a_{lm}|^2 \right\rangle + \left\langle |b_{lm}|^2 \right\rangle = 2\left\langle |a_{lm}|^2 \right\rangle = 2\left\langle |b_{lm}|^2 \right\rangle = 2\Sigma_l \tag{12}$$

Eq. (7) can then be rewritten as

$$\partial_t X_{lm} = -\tau_l^{-1} X_{lm} + a_{lm}(t) \tag{13}$$

and similarly for Y_{lm}. As Eq. (13) is a simple Langevin equation, the exact time update [27] is given as

$$X_{lm}(t+\Delta t) = X_{lm}(t) e^{-\Delta t/\tau_l} + \left[\frac{1}{2}\Sigma_l^2 \tau_l \left(1 - e^{-2\Delta t/\tau_l}\right)\right]^{1/2} n \tag{14}$$

such that Δt is the time step size and n is a sample value from the normal distribution $\mathcal{N}(0,1)$. In order to properly resolve the dynamics of the higher order coefficient, a sufficiently small time step must be chosen so that $\Delta t << \tau_{l_{\max}}$. Yet as each harmonic coefficient is independent of each other, Eq. 14 can be evaluated for all X_{lm} and Y_{lm} simultaneously. Given all the harmonic coefficients (f_{lm}), the cross-section at the equator, $R(\theta = \pi/2)$, can easily be computed using Eq. (4).

When running the numerical simulations, the user has some choice of which input parameters to specify. For example, one can specify the effective surface tension (dimensionless) $\bar{\sigma}$ and the largest incorporated mode l_{max}. In this case, the vesicle's excess is obtained from [23]

$$\alpha = \frac{\mathrm{k}_B T}{2\kappa}\left[\frac{5}{6+\sigma} + \ln\left(\frac{l_{max}^2 + \bar{\sigma}}{12 + \bar{\sigma}}\right)\right], \tag{15}$$

Alternatively, one can specify α and $\bar{\sigma}$, and Eq.(15) then provides the requisite l_{max}.

Here we demonstrate an example of a numerically simulated vesicle with predefined bending rigidity and membrane tension. Figure (S5)b shows a time sequence of equatorial vesicle contours with bending rigidity of $\kappa = 10^{-19}$ J and membrane tension of $\sigma = 10^{-9}$ N/m. The size of the vesicle is $R_0 = 10^{-5}$ m. By implementing our image detection technique and fitting algorithm from *Gracia et al.*[3], we are able to reproduce the bending rigidity and membrane tension respectively as $\kappa = (1.00 \pm 0.01) \times 10^{-19}$ J and $\sigma = (1.1 \pm 0.2) \times 10^{-9}$ N/m with the Helfrich spectrum given in Figure (S5). Notably our image detection is able to resolve more than 45 shape fluctuation modes.

Simulating the Effect of Out-of-focus Signal

Due to a finite focal depth, the microscope imaging does not capture only the optical/fluorescence signal at the focal (equatorial) plane. The out-of-focus signal results in gradient in the image intensity near the focal plane vesicle contour.

To simulate this effect, we numerically projected the vesicle shape $R(\theta, \phi, t)$ on the equatorial plane and assigned intensity of the projected location, $R(\theta, \phi, t)\sin\theta$, given by

$$I(r, \phi, t) = \int_0^{2\pi} \int_{\frac{\pi}{2}-\theta_{fd}}^{\frac{\pi}{2}+\theta_{fd}} W(\theta')\ \delta(\phi - \phi')\ \delta(r - R(\theta', \phi', t)\sin\theta')\ d\theta' d\phi', \tag{16}$$

where $\frac{\pi}{2} \pm \theta_{fd}$ are the top and bottom of the microscope focal depth (FD), $\theta_{fd} = \arctan(FD/R_0)$. $W(\theta)$ is the intensity weighting function

$$W(\theta) = \frac{1}{W_0}\exp\left[-\frac{\cos^2(\theta)}{2\cos^2(\theta_{fd})}\right] \tag{17}$$

and W_0 is the corresponding normalization constant. The resulting images of the equatorial plane at different focal depth are illustrated in Figure S6a.

We varied the magnitude of the focal depth FD, from 0 to $0.3R_0$. The fluctuation spectra obtained for the simulations are shown in Figure S6b for a vesicle sized $R_0 = 20\,\mu m$ with κ= 22 $\mathrm{k}_B T$ and $\sigma = 1.4\times10^{-9}$ N/m. The crossover mode $q_c = \sqrt{\bar{\sigma}} \sim 3$. The effect of the projections is only significant for modes $q \geq \Delta^{-1}$, where $\Delta = \frac{FD}{R_0}$ [10]. For smaller values of $\Delta < 0.05$, the projections have no effect - the spectra overlap implying same bending rigidity. However, as the value of Δ increases, more modes get affected by the projections resulting in an effective softening of the membrane from 22 $\mathrm{k}_B T$ to 19 $\mathrm{k}_B T$, see S6c.

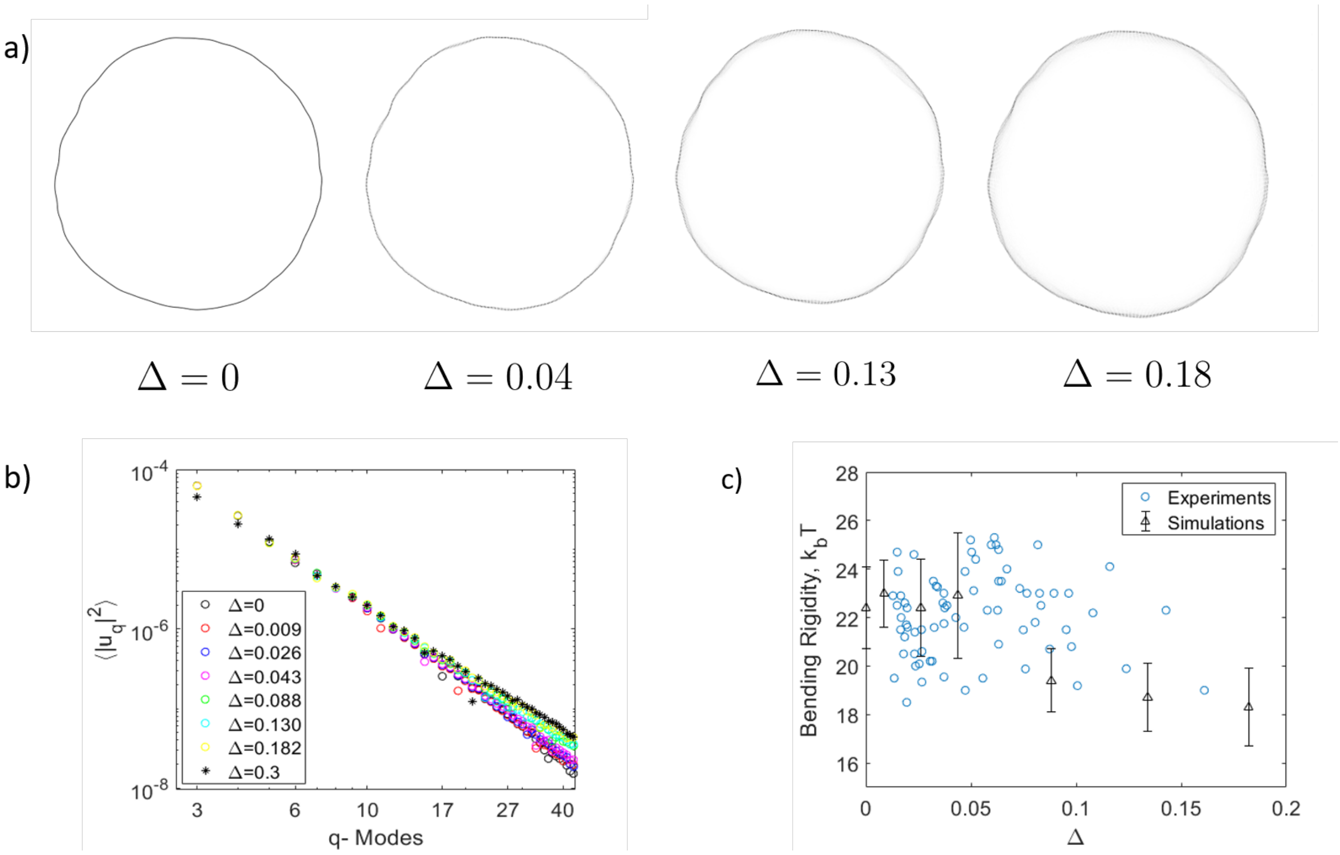

Fig. S 6: a) Snapshot of vesicle equatorial contours at different $\Delta = FD/R_0$. The simulated vesicle has bending rigidity= 22 $\mathrm{k}_B T$, membrane tension= 1.4×10^{-9} N/m and radius $R_0 = 20\,\mu m$. Each image was acquired over 0.2 s (corresponding to imaging rate of 5 fps). b) Fluctuation spectrum obtained at different Δ from the numerical simulations c) Bending rigidity obtained for different Δ. Here we have compared the experimental results with numerical simulations.

Fluctuations statistics: derivations of the basic results

Here we summarize the main results for the dynamics of a quasi-spherical vesicle.

Mean Squared Magnitude of the Fourier Modes: The dynamics of the spherical harmonics modes is governed by the following Langevin equation,

$$\frac{\partial f_{lm}}{\partial t} = -\tau_l^{-1}\, f_{lm} + \zeta_{lm} \tag{18}$$

where the relaxation time τ_l is given by Eq.(9) and the noise is

$$\left\langle \zeta_{lm} \right\rangle = 0 \text{ and } \left\langle \zeta^*_{lm}(t)\zeta_{l'm'}(t') \right\rangle = \frac{2\mathrm{k}_B T \Gamma_l}{\eta_{\mathrm{ex}} R_0^3}\delta(t-t')\delta_{ll'}\delta_{mm'}. \tag{19}$$

The analytic solution to Eq. (18) is given by

$$f_{lm}(t) = e^{-t/\tau_l} f_{lm}(0) + \int_0^t e^{-(t-t')/\tau_l} \zeta_{lm}(t') dt'. \tag{20}$$

and therefore

$$|f_{lm}(t)|^2 = e^{-2t/\tau_l} |f_{lm}(0)|^2 + \int_0^t e^{-(2t-t')/\tau_l} \Big(f_{lm}(0)\zeta^*_{lm}(t') + f_{lm}(0)^* \zeta_{lm}(t') \Big) dt' + \int_0^t \int_0^t e^{-(2t-t'-t'')/\tau_l} \zeta_{lm}(t')\zeta^*_{lm}(t'') dt' dt''. \tag{21}$$

The ensemble average of $\Big\langle |f_{lm}|^2 \Big\rangle$ of Eq. (21) is then

$$\Big\langle |f_{lm}|^2 \Big\rangle = e^{-2t/\tau_l} |f_{lm}(0)|^2 + \int_0^t e^{-(2t-t')/\tau_l} \left(f_{lm}(0) \Big\langle \zeta^*_{lm}(t') \Big\rangle + f_{lm}(0)^* \Big\langle \zeta_{lm}(t') \Big\rangle \right) dt' + \int_0^t \int_0^t e^{-(2t-t'-t'')/\tau_l} \Big\langle \zeta_{lm}(t')\zeta^*_{lm}(t'') \Big\rangle dt' dt''. \tag{22}$$

Using Eq. (19), Eq. (22) simplifies to

$$\Big\langle |f_{lm}|^2 \Big\rangle = e^{-2t/\tau_l} |f_{lm}(0)|^2 + \frac{2\mathrm{k}_B T \Gamma_l}{\eta_{\mathrm{ex}} R_0^3} \int_0^t e^{-2(t-t')/\tau_l} dt'. \tag{23}$$

$$\Big\langle |f_{lm}|^2 \Big\rangle = e^{-2t/\tau_l} |f_{lm}(0)|^2 + \frac{\mathrm{k}_B T \Gamma_l \tau_l}{\eta_{\mathrm{ex}} R_0^3} \Big[1 - e^{-2t/\tau_l} \Big] \tag{24}$$

At long times, $t >> \tau_l$, Eq. (24) simplifies to

$$\Big\langle |f_{lm}|^2 \Big\rangle = \frac{\mathrm{k}_B T \Gamma_l \tau_l}{\eta_{\mathrm{ex}} R_0^3} = \frac{k_B T}{\kappa} \Big[(l+2)(l-1)\Big(l(l+1) + \bar{\sigma} \Big) \Big]^{-1} \tag{25}$$

Recall $\bar{\sigma} = \sigma R_0^2/\kappa$. Since the dynamics of the different spherical harmonics modes are completely decoupled, we can more generally say

$$\Big\langle f^*_{lm} f_{l'm'} \Big\rangle = \frac{k_B T \Gamma_l \tau_l}{\eta_{\mathrm{ex}} R_0^3} = \frac{k_B T}{\kappa} \Big[(l+2)(l-1)\Big(l(l+1)\kappa + \bar{\sigma} \Big) \Big]^{-1} \delta_{ll'} \delta_{mm'} \tag{26}$$

Next, we consider the contour of the GUV at the equator as a function of the spherical harmonic coefficients:

$$r(\phi, t) = R_0 \left(1 + \sum_{q=0}^{q_{\max}} u_q(t) e^{\mathrm{i}q\phi} \right) = R_0 \Big(1 + \sum_{l=0}^{l_{\max}} \sum_{m=-l}^{l} f_{lm}(t) \mathcal{Y}_{lm}(\pi/2, \phi) \Big). \tag{27}$$

The Fourier coefficient for the q-th mode is then given by

$$u_q(t) = \frac{1}{2\pi R_0} \int_0^{2\pi} r(\phi, t) e^{-iq\phi} d\phi = \sum_{l=q}^{l_{\max}} f_{lq}(t) \left(n_{lq} P_{lq}(0) e^{\mathrm{i}q\phi} \right) e^{-\mathrm{i}q\phi} \tag{28}$$

as all the other terms integrate to zero. In the above equation, we have inserted the definition of the spherical harmonic, $\mathcal{Y}(\theta, \phi) = n_{lm} P_{lm}(\cos\theta) e^{\mathrm{i}m\phi}$ (see Eq.(5)), which shows that the dependence on ϕ cancels out.

The mean squared amplitude of u_q is then given by

$$\langle |u_q|^2 \rangle = \sum_{l=q}^{l_{\max}} \sum_{l'=q}^{l_{\max}} \langle f^*_{l'q} f_{lq} \rangle n_{lq} n_{l'q} P_{lq}(0) P^*_{l'q}(0). \tag{29}$$

Using Eq. (26), the above equation simplifies to

$$\left\langle |u_q|^2 \right\rangle = \sum_{l=q}^{l_{\max}} \langle |f_{lq}|^2 \rangle n_{lq}^2 |P_{lq}(0)|^2 \tag{30}$$

$$\left\langle |u_q|^2 \right\rangle = \mathrm{k}_B T \sum_{l=q}^{l_{\max}} \left[(l+2)(l-1)\Big(l(l+1)\kappa + \sigma R_0^2 \Big) \right]^{-1} n_{lq}^2 |P_{lq}(0)|^2 \tag{31}$$

Eq.(31) follows q^{-3} behavior for bending dominated modes $q > \sqrt{\bar{\sigma}}$ (and q^{-1} behavior for tension dominated modes $q < \sqrt{\bar{\sigma}}$).

Time Correlation for Fourier Modes: Time correlations present another useful metric to analyze the membrane fluctuations. As the different spherical harmonics modes are independent, the average time correlations,

$$\Big\langle u_q(0) u_q^*(t) \Big\rangle = \sum_{l'=|q|}^{l_{max}} \sum_{l''=|q|}^{l_{max}} \Big\langle f_{l'q}(0)\ f_{l''q}^*(t) \Big\rangle n_{l'q} n_{l''q} P_{l'q}(0)\ P_{l''q}^*(0), \tag{32}$$

can be simplified to

$$\Big\langle u_q(0) u_q^*(t) \Big\rangle = \sum_{l=|q|}^{l_{max}} \Big\langle f_{lq}(0)\ f_{lq}^*(t) \Big\rangle n_{lq}^2 \Big| P_{lq}(0) \Big|^2 , \tag{33}$$

Using (21), (32) can be rewritten as

$$\Big\langle u_q(0) u_q^*(t) \Big\rangle = \sum_{l=|q|}^{l_{max}} \Big\langle |f_{lq}|^2 \Big\rangle n_{lq}^2 \Big| P_{lq}(0) \Big|^2 e^{-t/\tau_l}. \tag{34}$$

Since the first term in (34) has both the smallest decay rate (τ_q^{-1}) and largest mean-squared amplitude, the time correlation can be approximated to leading order as

$$\Big\langle u_q(0) u_q^*(t) \Big\rangle = \Big\langle |f_{qq}|^2 \Big\rangle n_{qq}^2 \Big| P_{qq}(0) \Big|^2 e^{-t/\tau_q}. \tag{35}$$

If we consider limit of undulations with short wavelengths (shorter than the vesicle radius), $q \gg 1$, then the leading order decay rate can be approximated as

$$\tau_q^{-1} \approx \frac{q^3 R_0^{-3}\kappa + q R_0^{-1}\sigma}{2(\eta_{\mathrm{ex}} + \eta_{\mathrm{in}})} = \frac{\kappa}{\eta_{\mathrm{ex}} R_0^3} \frac{q^3 + q\bar{\sigma}}{2(1+\lambda)} \tag{36}$$

which is the decay rate derived using planar fluctuations. However, we suggest using the exact decay rate from the spherical harmonics as it is both more accurate and valid for all Fourier modes.

When comparing the time correlations in Fig.7, the exact decay rate, from the full spherical harmonics (SpH), is immediately more accurate than if the planar membrane (PM) decay rate is used. To get the accuracy even better, the higher order terms in Eq. (34) must be included. If all of the terms are included then the time correlation is directly on top of the curve from produced by the numerical simulation. However, as it is not feasible to include all the terms for real membranes, it is of interest to know how many terms are enough to sufficiently reproduce the numerical simulations. As shown in Figure 5, the time correlation produced by including the first two terms in Eq. (34 lies almost directly on top of the true solution. Including more terms would improve the accuracy further, but it is not likely to be significant due to experimental error.

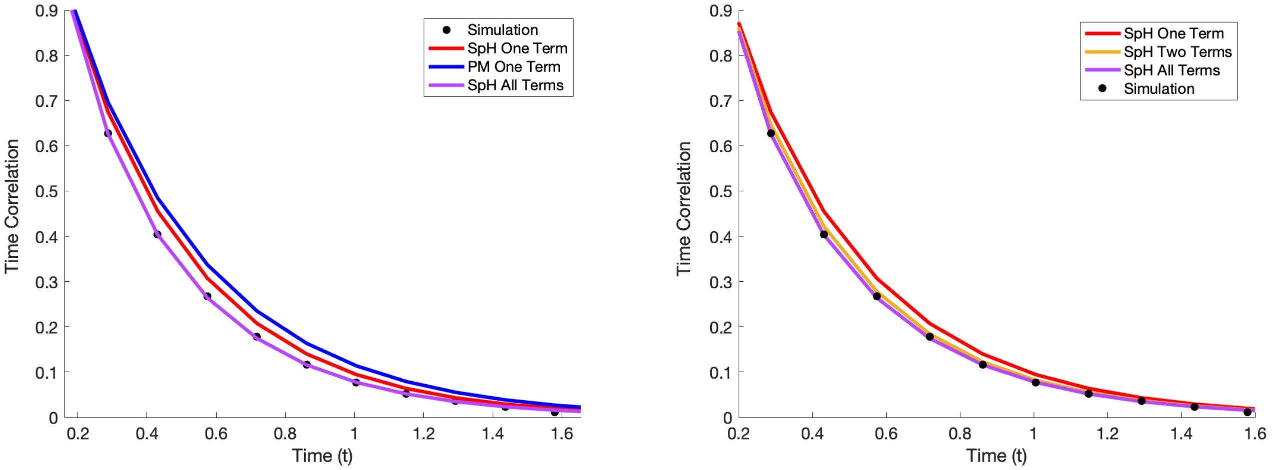

Fig. S 7: Plots comparing the analytic approximations for time correlation for Fourier mode $q = 5$. The left plots the time correlations using the exact spherical harmonic (SpH) decay rate and the less accurate planar membrane (PM) decay rate. The right plots the time correlations for the SpH case using different number of terms. The black dots show the time correlations computed from a numerical simulation using the following parameters as inputs. $R_0 = 3 \times 10^{-5}$ m, $\kappa = 5 \times 10^{-19}$ J, $\sigma = 4 \times 10^{-8}$ N/m, $l_{max} = 14$

Cross-Spectral Density: Similar to time correlations, the Cross-Spectral Density (CSD) is given by

$$\Big\langle |u_q(0)||u_q(t)| \Big\rangle - \Big\langle |u_q|^2(0) \Big\rangle. \tag{37}$$

For the sake of clarity of explanation, in this section we will use the leading order approximation of u_q,

$$u_q(t) \approx f_{qq}(t) n_{qq} P_q \left(\cos \frac{\pi}{2} \right) . \tag{38}$$

Using (20), this can be rewritten as

$$u_q(t) = e^{-t/\tau_l} u_q(0) + \bar{\zeta}_q(t), \tag{39}$$

where

$$\bar{\zeta}_q = n_{qq} P_{qq}(0) \int_0^t e^{-(t-t')/\tau_l} \zeta_{lm}(t') dt'$$

is a random normally distributed Weiner process.

From (39), it is clear that $u_q(t) = \bar{\zeta}_q(t)$ for large values of t. Furthermore, it is worth noting that all Fourier modes, except $q = 0$, have both real and an imaginary component, $u_q = A_q + \mathrm{i}B_q$, and that these two components are independent of each other. Likewise, the thermal noise can be decomposed into independent real and imaginary components: $\bar{\zeta}_q = \bar{\zeta}_{Aq} + \mathrm{i}\bar{\zeta}_{Bq}$. The real component of Eq. (39) can then be written as

$$A_q(t) = A_q(0) e^{-t/\tau_q} + \bar{\zeta}_{Aq}(t) \tag{40}$$

and a similar expression for B_q.

Therefore, it can be shown that

$$\begin{aligned} \Big\langle |u_q(0)||u_q(t)| \Big\rangle &= \Big\langle |u_q(0)| \Big(A_q^2(t) + B_q^2(t) \Big)^{1/2} \Big\rangle \\ &= \Big\langle |u_q(0)| \Big(|\bar{\zeta}_q|^2(t) + 2\big(\bar{\zeta}_{Aq}(t) A_q(0) + \bar{\zeta}_{Bq}(t) B_q(0) \big) e^{-t/\tau_q} + |u_q(0)|^2 e^{-2t/\tau_q} \Big)^{1/2} \Big\rangle \end{aligned} \tag{41}$$

If we assume that $t >> t_q$, then we can perform the following expansion

$$\begin{aligned}\Big\langle |u_q(0)||u_q(t)| \Big\rangle = \Big\langle |u_q(0)| \Big\rangle \Big\langle |\bar{\zeta}_q(t)| \Big\rangle \\ + \left(\Big\langle |u_q(0)| A_q(0) \Big\rangle \Big\langle \frac{\bar{\zeta}_{Aq}(t)}{|\bar{\zeta}_q(t)|} \Big\rangle + \Big\langle |u_q(0)| B_q(0) \Big\rangle \Big\langle \frac{\bar{\zeta}_{Bq}(t)}{|\bar{\zeta}_q(t)|} \Big\rangle \right) e^{-t/\tau_q} \\ + \frac{1}{2} \left(\frac{\Big\langle |u_q(0)|^3 \Big\rangle}{\Big\langle |\bar{\zeta}_q(t)| \Big\rangle} - \Big\langle \frac{|u_q(0)| \big(\bar{\zeta}_{Aq}(t) A_q(0) + \bar{\zeta}_{Bq}(t) B_q(0) \big)^2}{|\bar{\zeta}_q(t)|^3} \Big\rangle \right) e^{-2t/\tau_q} + \mathcal{O}\big(e^{-3t/\tau_q}\big). \end{aligned} \tag{42}$$

The second term in (42) averages to zero due to the thermal noise factor. Therefore, to leading order, the CSD is given as

$$\Big\langle |u_q(0)||u_q(t)| \Big\rangle - \Big\langle |u_q(0)| \Big\rangle^2 = C_q e^{-2t/\tau_q} + \mathcal{O}\big(e^{-3t/\tau_q}\big) \tag{43}$$

where C_q is a normalization constant.

Therefore, the slowest decaying mode of the CSD is $\mathcal{O}\big(e^{-2t/\tau_q}\big)$. This contradicts H. Zhou et al. [11] who give it as $\mathcal{O}\big(e^{-t/\tau_q}\big)$. This factor of two is a consequence that each Fourier coefficient has both a real and imaginary component that are completely independent of each other.

Finally, users are recommended to use time correlations over CSD. CSD requires the same amount of work and contains the same higher order error as the time correlation method. Yet, CSD has an additional layer of truncation error introduced in the expansion in Eq.(42).

Movie S1

Real-time video of the GUV from Figure 1 in the main text (DOPC labeled with 0.2 mol % TR-DHPE) acquired with phase contrast microscopy. The vesicle radius is 29.6 μm.

Movie 2

Video of the GUV from Figure 1 in the main text (DOPC labeled with 0.2 mol % TR-DHPE) acquired with confocal microscopy. The objective used is 40x/0.6 NA with the pinhole size 1 A.U. The polarization effect was corrected by using circular rotation plates to have even intensities across the equatorial vesicle plane. The vesicle radius is 29.6 μm.

Movie S3

Real time video of the GUV from Figure 6 in the main text consisting of DOPC labeled with TR DHPE (0.8%) acquired with confocal microscopy. The objective used is 40x/0.6 NA at 13.2 fps with the pinhole size 1 A.U. The polarization effect was corrected by using circular rotation plates to have even intensities across the equatorial vesicle plane.

Raw data

Raw data are available at `https://dx.doi.org/10.17617/3.4p`. This collection of raw data, consists of 4 folders each containing zipped files of data.

In folder “Raw data - Fourier modes”, 2 different sets of experimental data are included: phase contrast (PC) and confocal (C) microscopy on the same vesicle and confocal microscopy data with different pinhole sizes. The folder contains excel sheets with fluctuation amplitude for every Fourier mode and the metadata with all the microscopy conditions. The vesicles have different sizes so that they practically cover a good span of focal depth (Δ) from 0.03 to 0.15. The meta data is included in the first sheet of the excel file. The second sheet has the mode and mean squared amplitude (and error). The remaining sheets have the Fourier modes for every microscopy setting (and focal depth). Note that our Fourier signal was normalized by vesicle radius. For the definition of our Fourier transform, please refer to *Gracia et al.*[3]. The contour detection is conducted as given in the main text and supplement.

The rest of the folders as listed below contain vesicle images in tiff format (grouped in folders for the separate vesicle as suggested by the folder name) and an excel sheet with the meta data indicating the specific microscopy conditions (AU = Airy unit, NA = numerical aperture).

The folder “Raw images - different focal depth” contains confocal microscopy raw images at different focal depths without any image processing for vesicles of different sizes.

The folder “Raw images - phase contrast vs confocal” contains phase contrast and confocal microscopy raw images for the same vesicle without any image processing for vesicles of different sizes.

The folder “Raw images - polarization correction” contains polarized and polarization-corrected confocal microscopy raw images for the same vesicle without any image processing.

---

[1] R. Dimova. Recent developments in the field of bending rigidity measurements on membranes. Adv. Coll. Int. Sci., 208:225–234, 2014.

[2] Joanna B. Dahl, Vivek Narsimhan, Bernardo Gouveia, Sanjay Kumar, Eric S. G. Shaqfeh, and Susan J. Muller. Experimental observation of the asymmetric instability of intermediate-reduced-volume vesicles in extensional flow. Soft Matter, 12:3787–3796, 2016.

[3] R. S. Gracia, N. Bezlyepkina, R. L. Knorr, R. L. Lipowsky, and R. Dimova. Effect of cholesterol on the rigidity of saturated and unsaturated membranes: fluctuation and electrodeformation analysis of giant vesicles. Soft Matter, 6:1472-1482, 2010.

[4] Yuval Elani, Sowmya Purushothaman, Paula J. Booth, John M. Seddon, Nicholas J. Brooks, Robert V. Law, and Oscar Ces. Measurements of the effect of membrane asymmetry on the mechanical properties of lipid bilayers. Chem. Commun., 51:6976–6979, 2015.

[5] Dinesh Kumar, Channing M. Richter, and Charles M. Schroeder. Conformational dynamics and phase behavior of lipid vesicles in a precisely controlled extensional flow. Soft Matter, 16:337–347, 2020.

[6] Aidan T. Brown, Jurij Kotar, and Pietro Cicuta. Active rheology of phospholipid vesicles. Phys. Rev. E, 84:021930, Aug 2011.

[7] Arwen I. I. Tyler, Jake L. Greenfield, John M. Seddon, Nicholas J. Brooks, and Sowmya Purushothaman. Coupling phase behavior of fatty acid containing membranes to membrane bio-mechanics. Frontiers in Cell and Developmental Biology, 7:187, 2019.

[8] Sowmya Purushothaman, Pietro Cicuta, Oscar Ces, and Nicholas J. Brooks. Influence of high pressure on the bending rigidity of model membranes. The Journal of Physical Chemistry B, 119(30):9805–9810, Jul 2015.

[9] P Shchelokovskyy, S Tristram-Nagle, and R Dimova. Effect of the HIV-1 fusion peptide on the mechanical properties and leaflet coupling of lipid bilayers. New Journal of Physics, 13(2):025004, feb 2011.

[10] S. Alex Rautu, Davide Orsi Lorenzo Di Michele, George Rowlands Pietro Cicuta and Matthew S. Turner. The role of optical projection in the analysis of membrane fluctuations. Soft. Matter., 17, 2017 3480-3483.

[11] H. Zhou, B. B. Gabilondo, W. Losert, and W. van de Wate. Stretching and relaxation of vesicles. Phys. Rev. E, 83:011905, 2011.

[12] W. Rawicz, K.C. Olbrich, T. McIntosh, D. Needham, and E. Evans. Effect of chain length and unsaturation on elasticity of lipid bilayers. Biophys. J., 79:328–339, 2000.

[13] Jianjun Pan, Stephanie Tristram-Nagle, Norbert Kučerka, and John F. Nagle. Temperature dependence of structure, bending rigidity, and bilayer interactions of dioleoylphosphatidylcholine bilayers. Biophysical Journal, 94(1):117–124, Jan 2008.

[14] M. S. Jablin, K. Akabori, and J. F. Nagle. Experimental support for tilt-dependent theory of biomembrane mechanics. Phys. Rev. Lett., 113:248102, Dec 2014.

[15] B. Sorre, A. Callan-Jones, J.-B. Manneville, P. Nassoy, J.-F. Joanny, J. Prost, B. Goud, and P. Bassereau. Curvature-driven lipid sorting needs proximity to a demixing point and is aided by proteins. PNAS, 106:5622–5626, 2009.

[16] Sudipta Gupta, Judith U. De Mel, Rasangi M. Perera, Piotr Zolnierczuk, Markus Bleuel, Antonio Faraone, and Gerald J. Schneider. Dynamics of phospholipid membranes beyond thermal undulations. The Journal of Physical Chemistry Letters, 9(11):2956–2960, Jun 2018.

[17] Judith U. De Mel, Sudipta Gupta, Rasangi M. Perera, Ly Ngo, Piotr Zolnierczuk, Markus Bleuel, Sai Venkatesh Pingali, and Gerald J. Schneider. Influence of salt on membrane rigidity of neutral DOPC vesicles. Langmuir, 36:9356–9367, 2020.

[18] T. Betz, and C. Sykes. Time resolved membrane fluctuation spectroscopy. Soft. Matter., 8, 2012 5317-5326.

[19] Miglena I. Angelova and Dimiter S. Dimitrov. Liposome electroformation. Faraday Discuss. Chem. Soc., 81:303–311, 1986.

[20] K. K. Scott E. Maxwell, Harold D. Delaney, Designing Experiments and Analyzing Data: A Model Comparison Perspective, Taylor and Francis, 3rd edn., 2017

[21] Michael Chernick. Bootstrap Methods: A Guide for Practitioners and Researchers. John Wiley & Sons, Inc., 2 edition, 2007.

[22] U. Seifert. Configurations of fluid membranes and vesicles. Advances in physics, 46:13–137, 1997.

[23] U. Seifert. Fluid membranes in hydrodynamic flow fields: Formalism and an application to fluctuating quasispherical vesicles. Eur. Phys. J. B, 8:405–415, 1999.

[24] P. M. Vlahovska. Dynamics of membrane bound particles: capsules and vesicles. In C. Duprat and H.A. Stone, editors, Low-Reynolds-Number Flows: Fluid-Structure Interactions. Royal Society of Chemistry Series RSC Soft Matter, 2016.

[25] Petia M. Vlahovska and C. Misbah. Theory of vesicle dynamics in flow and electric fields. In R. Dimova and C. Marques, editors, The Giant Vesicle Book, page Chapter 7. CRC Press, 2019.

[26] S. T. Milner and S. A. Safran. Dynamical fluctuations of droplet microemulsions and vesicles. Phys. Rev. A, 36:4371–4379, 1987.

[27] D. Gillespie. Exact numerical simulation of the Ornstein-Uhlenbeck process and its integral. Physical Review E, 54, 1996 2084-2091.